Post-Process Frequency Tuning of Single-Mode Quantum Cascade Laser at 4.7 THz

Tudor Olariu[ID], Mattias Beck[ID], and Jérôme Faist, *Fellow, IEEE*

Abstract— **We present a systematic study of the optical design, fabrication, and characterization of quantum cascade laser devices with a frequency around 4.7 THz, intended for use as local oscillators in the GREAT heterodyne receiver aboard SOFIA (Heyminck, et al., 2012), (Risacher et al., 2018). The measured devices exhibit consistent spectral performance, with approximately 75% of them having their emission frequency within a 6 GHz band relative to their nominal value. We present surface-emitting lasers capable of covering the required 4743-4748 GHz frequency interval, with powers up to 2.2mW at 40K in continuous wave. Their emission frequency can be tuned up to +2 GHz with current over 80mA and -5 GHz over the 20-60K range with temperature. Additionally, we explain how processing variability is exploited to shift the emission frequency post-process and post-measurement: occurring during an etching step, the undesired height difference between different sample areas can be minimized using custom thicknesses for depositing various materials. This alters the effective refractive index of the optical mode, thus changing the laser's emission frequency.**

Index Terms— **Terahertz (THz), quantum cascade lasers (QCL), frequency tuning, microfabrication.**

I. INTRODUCTION

THE terahertz (THz) range of the electromagnetic spectrum has been of increasing interest for researchers, due to both its technological and scientific relevance. Owing to the advantages of THz radiation [1] - the existence of spectral signatures enabling THz waves to detect concealed materials and explosives [2], its capability of probing biological tissue [3], its favorable properties in communication technology and spectroscopy [4] - this frequency range is especially suited for imaging applications. In particular, fields such as observational astronomy are concerned with this frequency region, as many atomic cooling lines and molecular rotational and vibrational lines are situated here [5], [6], [7]. Observing the radiation originating in space can help gain an understanding regarding astrophysical processes, such as characterizing the galactic interstellar medium, evolution of the early universe or the conditions of star formation, by investigating their chemical compositions through various atomic and molecular species.

To this end, since the spectral lines are well defined, a heterodyne measurement setup can be used, where the incoming signal is mixed with a local oscillator of precisely controlled frequency. Terahertz quantum cascade lasers (QCL) [8], [9] are prime candidates for such a role, given their frequency span, compactness and high achievable output power [10], [11], [12], [13], [14], [15], [16], [17], [18], [19], for both ground based and airborne [20], [21], [22], [23] laboratories, while significant progress is also being done towards their high temperature operation [24], [25], [26].

One target frequency is 4.745 THz, representing the [OI] cooling line [27]. This work presents the development of a THz QCL with the purpose of a local oscillator at this frequency, by emitting a single mode with a near-Gaussian shaped far field pattern, covering a tuning range of ~5 GHz (to account for the potential frequency shift due to moving sources) and being powerful enough (required power ≥1mW) to pump the array of hot electron bolometers (HEB) [28] in GREAT setup [5], [6] for which they are designed. It is based on a bound-to-continuum heterostructure [29] that has been rescaled and iterated upon [30], [31], [32], [33], resulting in a measured threshold current density of $J_{th} = 137A/cm^2$.

II. DESIGN AND FABRICATION

The design of the laser is based on the approach first described in [31] and improved in [33]. It involves combining several elements in order to fulfill the required criteria: high output power (several milliWatts), single-mode operation (at 4.745 THz) with good mode control, surface emission, Gaussian far field pattern, low power dissipation. Each section has been optimized by 3D simulations. The main cavity is a 55.5 μm wide metal-metal waveguide [35], [36], with a 3.5 μm deep lateral corrugation alternating on either side. This second order grating has a period of 17.1 μm and has the purpose of introducing losses to higher order lateral modes (the 2nd lateral mode incurs grating losses of 1.44cm^{-1}), while affecting the fundamental one much less (loss for 1st lateral mode of 0.26cm^{-1}), thus promoting it to lase. The back mirror is a broadband distributed Bragg reflector (DBR) with high reflectivity (computed reflectivity >90%), centered around the target frequency, obtained by alternating two materials - the active region (for a length of ~4.3 μm) and a dielectric called Benzocyclobutene (length ~10.3 μm), for 4 periods of 14.6 μm each. Benzocyclobutene (abbreviated "BCB") is an insulating polymer, with a low refractive index (n≈1.55)
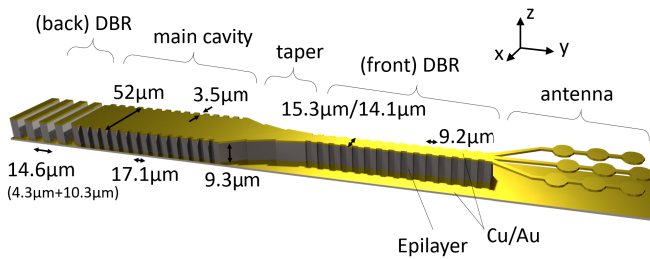
Fig. 1. 3D model of the laser, with all sections described in the text: back DBR, main cavity, taper, front DBR, antenna. Dimensions are indicated. The etched structure (depicted in gray) is surrounded by BCB (here not shown), making up the waveguide between the two metal layers (shown in yellow).

and low enough losses ($\alpha \approx$ 5-6cm^{-1}) around 4.7 THz, already used successfully in the THz range [31], [33], [37], [38].

The front distributed feedback mirror acts as a frequency selector, choosing the longitudinal Fabry-Pérot mode allowed in the cavity by decreasing the mirror losses only for a specific frequency mode. This is achieved by a first order lateral grating, calculated as a compromise between bandwidth, reflectivity and free spectral range: a longer cavity (of which the front DBR is a part, as the optical mode penetrates it to some depth) means a lower free spectral range, bringing the longitudinal modes closer together. This requires a narrower reflectivity bandwidth, in order to preserve single-mode operation. To achieve this, a smaller index contrast is needed (shallower corrugation), however this also causes a lower reflectivity. Eventually, this can be increased by adding more periods, which further elongates the cavity.

Thus, a period of 9.2 μm, with lateral widths of 15.3 μm and 14.1 μm (corrugation of 0.6 μm per side, which determines an index contrast of $\Delta n = 3.443-3.4099 = 0.0331$), was repeated 70 times to obtain the front DBR with a reflectivity of $\sim$35%. This front mirror is connected to the main cavity by a 3-section taper, again simulated to provide high transmission (>90%) only for the fundamental optical mode. The whole structure is embedded in the above-mentioned BCB, allowing the fabrication of the DBR in the back of the laser, as well as providing a platform to lay the patch array antenna, as the last component of the device. In this manner, the output coupler is an array of 3 × 3 dipole emitters [39], which provides a single-lobed far field pattern, while effectively being an extension of the top metallization of the waveguide. The entire device is illustrated in Fig.1.

The sample has been processed from a GaAs/AlGaAs material system wafer, grown to a thickness of 9.3 μm by molecular beam epitaxy (MBE), with a doped contact InGaAs layer above and below. When heated during the bonding process, InGaAs interdiffuses with the metal cladding of the waveguide, which increases the waveguide losses. To mitigate this effect, in this process the top InGaAs layer has been etched by mild ion milling, and a n-doped GaAs contact layer has been grown instead by MBE.

A 10nm tantalum - 500nm copper sequence was electron beam evaporated on both the epilayer and the doped, $\sim$350μm-thick GaAs substrate. The material was transferred to the substrate by thermo-compressive waferbonding for 60min at 300 °C with an applied pressure of 4.5MPa, followed by the annealing at 300 °C for 30min. With the future waveguide thus having its bottom metal cladding, the epilayer was uncovered by means of mechanical polishing and chemical etching (citric acid-based). The bottom InGaAs layer was then removed using a phosphoric acid/hydrogen peroxide solution. The active material was dry etched by inductively coupled plasma (ICP) with a H$_2$/Cl$_2$-chemistry recipe, using a $\sim$3μm-thick patterned silicon nitride mask. The BCB polymer was spun (50s at 5000rpm) and cured a total of 5 times (at 210 °C, except the last curing which was done at 250 °C), until the active structure is overcoated by $\sim$15 μm, and then etched by reactive ion etching (RIE) back down to the same level as the epilayer (planarization). The top metallization (including the antenna) is then electron beam evaporated as a stack of Ta 5nm/Cu 250nm/Ti 20nm/Au 50nm, acting as the waveguide top cladding as well as a wire bonding pad for electrically contacting the laser.

III. RESULTS

Fig. 2a presents the light - current - voltage characteristic of such a device. The observed output power is 2.5mW while operated in continuous wave at 40K. Fig. 2b depicts the single mode nature of the emission spectrum by plotting the normalized intensity (in logarithmic scale) over a broad frequency range, while in Fig. 2c it can be seen that the single mode emission can be shifted by 2 GHz towards higher values with increasing bias, due to the cavity pulling effect [34], and by 5 GHz towards the red via temperature tuning. Therefore, the laser is able to cover the required range of 4743-4748 GHz, and does not limit the receiver (the detector bandwidth is $\sim$4 GHz [6]). Because these two tuning effects act in opposite directions (increasing temperature redshifts, whereas cavity pulling blueshifts), the current tunability is less efficient at higher temperatures. A more detailed map of the frequency tuning with bias and temperature is shown in Fig. 2d, just above the cooling limit of the setup (T>37.5K).

Variation in exposure parameters and the dry etching undercut changed the size of the waveguide by up to $\sim$1 μm below the intended dimension, the effect of which is estimated in Fig. 3. On the epilayer described above (9.3 μm-thick), a waveguide narrower than designed can change the effective index by an estimated $\sim$0.03, which would cause a frequency offset of approximately +50 GHz. During the planarization step, if the BCB is etched below the active region (typical height differences lie within 0.5 μm over the whole sample, with maximum over-etchings of up to $\sim$2-2.5 μm), the frequency also changes, albeit by several GHz per each μm of height difference (see the different curves in Fig. 3). Finally, the largest effect is observed if the front DBR period is wrong, as an error of just 100nm is sufficient to cause the same 50 GHz offset.

To account for this variability, a chirp of ±1.5% in length around the nominal value was introduced on the photolithography mask, covering $\mp$70 GHz around the central value of 4745 GHz. Thus, each laser on the sample was slightly different in expected emission wavelength, while the process
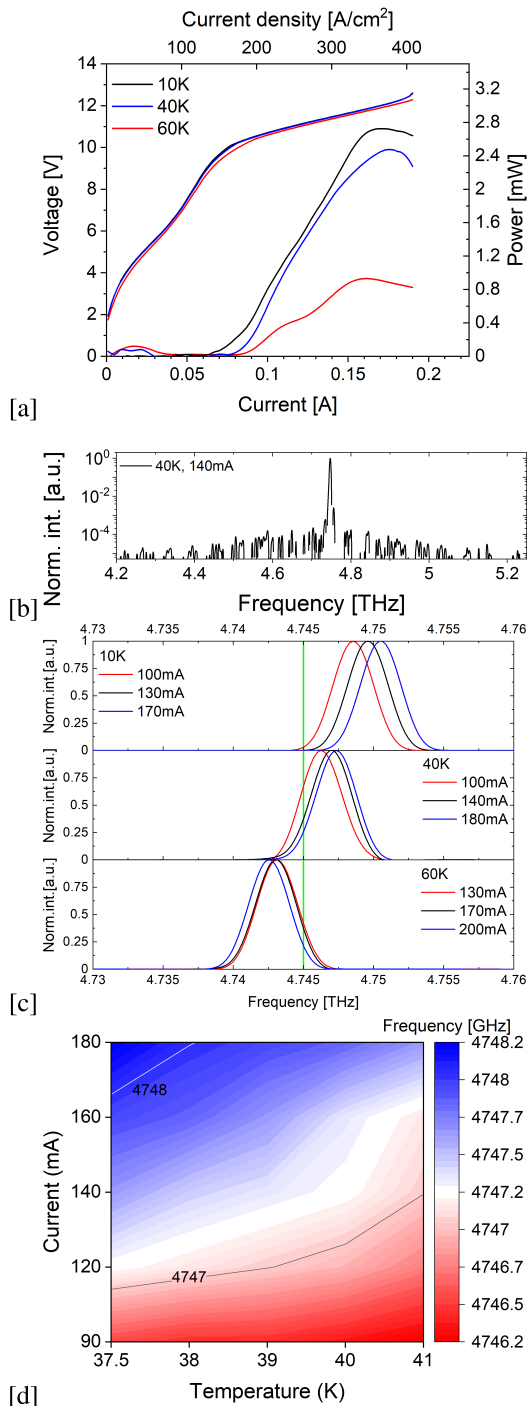
Fig. 2. a) Light-current-voltage characteristic of a measured laser. Output power above 2.8mW can be achieved. b) Log-scale spectrum showing single mode emission over a broad frequency range. c) Spectrum measurements at different biases and temperatures. In green, the target frequency, which is visibly covered by the tuning range of the laser. The inset shows the spectrum in logarithmic scale, displaying the single-mode characteristic over a large frequency range. d) Tuning map of the frequency as function of applied current and temperature, slightly above the target, as tuning to higher temperatures is preferred.

Fig. 3. Sensitivity of the effective index and emission frequency, based on common processing uncertainties. Effective index n_{eff} calculated as function of the height difference δ_{BCB} between the ridge and BCB, as well as the waveguide width. The reference index $n_{ref} = 3.4271$ was calculated for an average 14.7 μm-wide, 9.3 μm-tall waveguide. The axes on the right show the expected frequency for 3 different values of the front DBR period.

was able to cover a much larger range and therefore increasing the likelihood the target frequency was reached.

The plot on the left in Fig. 4 shows the measured frequency of several first generation devices against their designed frequency. The green horizontal line marks the target 4745 GHz, and the g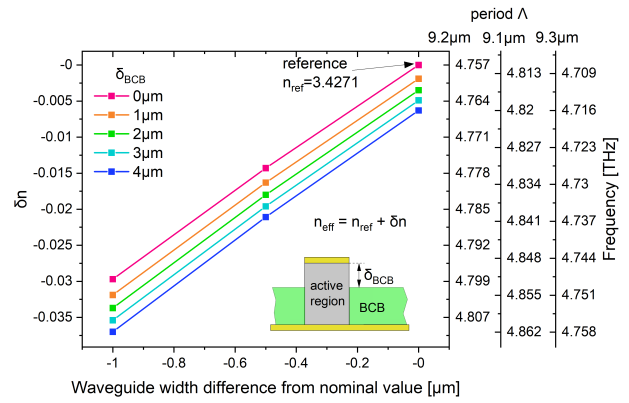rey area around it is the frequency range a laser should be able to cover. The black dashed line represents the points where a laser would emit at the intended frequency. However, the devices we measured form another, parallel line, ~76.42 GHz higher. This shift is likely caused by an undercut during the dry etching step (see Fig. 3) which changes the dimensions of the realized device compared to the photolithography mask and therefore, the emission frequency. To account for this phenomenon, the design was adjusted to compensate for the shift, by rigidly scaling all devices longitudinally (along y-axis in Fig. 1) by $\frac{76.42\ GHz}{4745 GHz} = 1.61\%$. Elongating the period of the front DBR causes the supported frequency to be pushed towards lower values and closer to the nominal one.

The right side of Fig. 4 shows the results obtained from the devices achieved using the updated $n_{eff} \approx 3.3731$. The data shows the correction overshot the intended effect, as most lasers now emit below their nominal frequency. However, this time the main trend contains 75% of measured devices and forms a band between 29 GHz and 36 GHz below the diagonal. Additionally, this band intersects the gray region, which represents the frequency range that must be covered by the ideal laser, centered around 4745 GHz. Because of processing edge effects, the devices situated within the last ~1mm from the edge of the sample are usually too low quality. This frame is marked as "quality edge" in Fig. 4 and acts as a frequency upper boundary for available lasers.

The consistent behavior of the devices can also be seen in the histograms from the insets of Fig. 4, which count their number as function of distance to their intended emission frequency, with a standard deviation of $\sigma = 1.484$ GHz and $\sigma = 1.415$ GHz respectively, for the two generations. The lower insets in the right figure further illustrate how all post-scaling devices start lasing between 80-90mA and have maximum output powers between 2-3mW.

A closer look at the histograms in Fig. 4 reveals a separation of $\delta\nu \approx 40$ GHz between two groups of modes, in both generations of devices. Writing $\delta\nu = \frac{c}{2n_g L}$ with $n_g \approx 4.1748$ yields an effective cavity length of $L \approx 0.9$mm, with the two mode groups likely corresponding to consecutive longitudinal modes
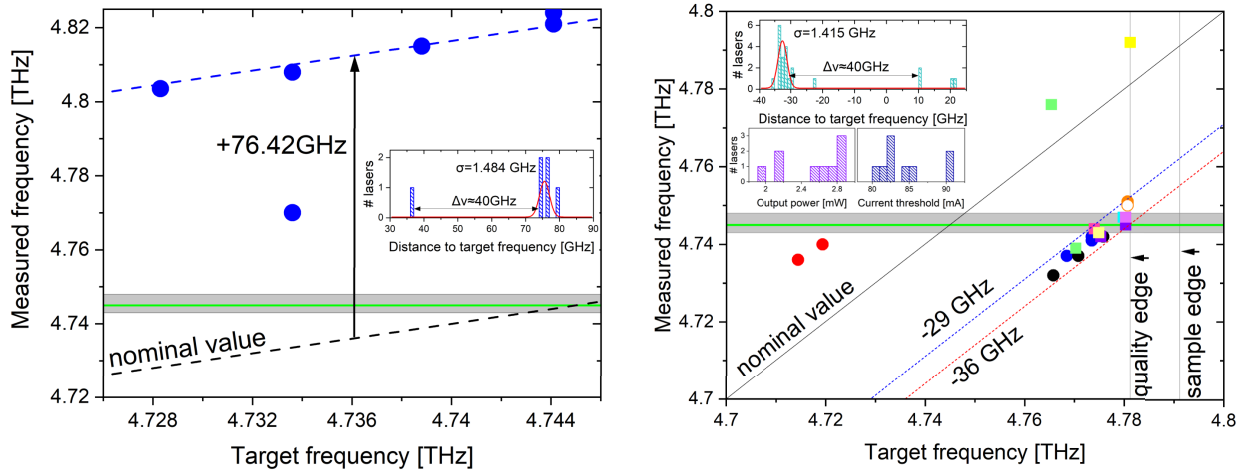
Fig. 4. Left: First generation of devices - measured frequency against target frequency. The horizontal green line is the desired frequency of 4745 GHz, the dashed line is the diagonal on which the measured value would equal the target one. The blue points have been measured, ~76.42 GHz higher than their nominal value. The inset depicts a statistic of measured lasers from the first generation, showing a distribution with $\sigma = 1.484$ GHz. Right: Second generation of devices - overview of measured lasers (each color represents a different sample that was measured, with each point signifying a separate device on that chip), after their linear length scaling by +1.61%. Ideally, data points would lie on the main diagonal (nominal value), however in this case they form a trend between 29 GHz and 36 GHz lower frequency. Their distribution is similar to the first generation, having $\sigma = 1.415$ GHz compared to $\sigma = 1.484$ GHz, albeit now shifted towards the red. Still, they overlap with the required frequency coverage band 4743-4748 GHz, shown in gray. The vertical lines on the right depict the quality edge (a margin of 1mm from the sample edge, unusable due to processing edge defects) and the sample edge, respectively. A histogram counting the second generation lasers that emit at different distances from their intended frequency is shown in the top inset. The multiple bars around 29-36 GHz correspond to ~75% of devices that were tested. Their distribution has a standard deviation of $\sigma = 1.465$ GHz, some of the devices lasing at the desired frequency (marked with a horizontal green line). The bottom insets show histograms of the current threshold (all devices start lasing between 80-90mA) and maximum output power (all values obtained 2-2.8mW).

inside the cavity. This means the scaling along y-axis of the DBR and the cavity should have been done by different factors in order to shift the main cavity mode towards the center of the DBR reflectivity band (since currently both generations are still detuned from the designed frequency, by +76 GHz and − [29], [30], [31], [32], [33], [34], [35], [36] GHz, respectively), thus obtaining a single mode family.

However, we are able to find devices with output powers of over 2mW (see Fig. 2a and the inset in Fig. 4), well above the requirement of 1mW, at precisely the required frequency, which can furthermore cover the necessary range 4743-4748 GHz (Fig. 2b,c).

IV. POST-PROCESS FREQUENCY ADJUSTMENT

One of the more delicate steps in the fabrication process is the planarization of the BCB, when dry etching is used to reduce the height of the polymer back to that of the active structure. Due to its viscosity, the BCB layer does not have the same height across the sample. This causes its etching to not happen uniformly over the sample, or even over a single device: some areas - typically the ends - are overetched, by the time the center of the laser is uncovered. A diagram of this height difference can be seen in the last panel of Fig. 5a.

The optical confinement of the mode, and therefore its effective index, is also affected by the uncertainty in the effective residual height of the BCB, as shown in Fig. 5b. Performing a 2D simulation of this effect reveals that a shift of several GHz can be induced in the emitted frequency if the polymer is etched a few micrometers below that intended height (see Fig. 5b). The curve naturally reaches a plateau towards the left, where the BCB level would remain above

the laser, as the optical mode does not see increasing amounts of polymer on top of the metal cladding.

In order to further explore this effect, and even exploit it, a laser which had a BCB step of slightly above 1 μm was found, marked with the gray line in Fig. 5b. The idea was to potentially frequency tune a device that has already been mounted and measured, entirely post-process, by adding back some polymer on top of the front mirror [41]. In this way, the optical mode is restored and the frequency shifted back, moving down the line and, assuming the grating will be completely submerged, even reach the left end of the curve.

Fig. 6 depicts such a mounted chip, with BCB (shown in green tint) applied over the front mirror of the devices (see inset). Care must be taken to not cover the antenna as well, since it would perturb the far field pattern. The laser was measured again and the single mode in the spectrum - see main Fig. 6 - was indeed shifted by about 5 GHz towards lower frequencies, as predicted by the simulation.

Another advantage of encasing the laser in BCB in this manner is the additional protection it offers, acting as a diffusion barrier against water vapor, residual air and impurities in the setup [40], especially around the front DBR. No known long term effects are caused by the thermal cycling of BCB - a study done over more than 10 cooling and heating cycles revealed no noticeable degradation and no change in the output frequency.

However, this effect can be extended to other materials as well, where a known refractive index can be used to refill, partially or totally, the active region - BCB height difference. In Fig. 7 we show the simulated red shift caused by depositing increasing amounts of silicon dioxide, given a certain initial δ_{BCB} value. In particular, we measured a laser before and after
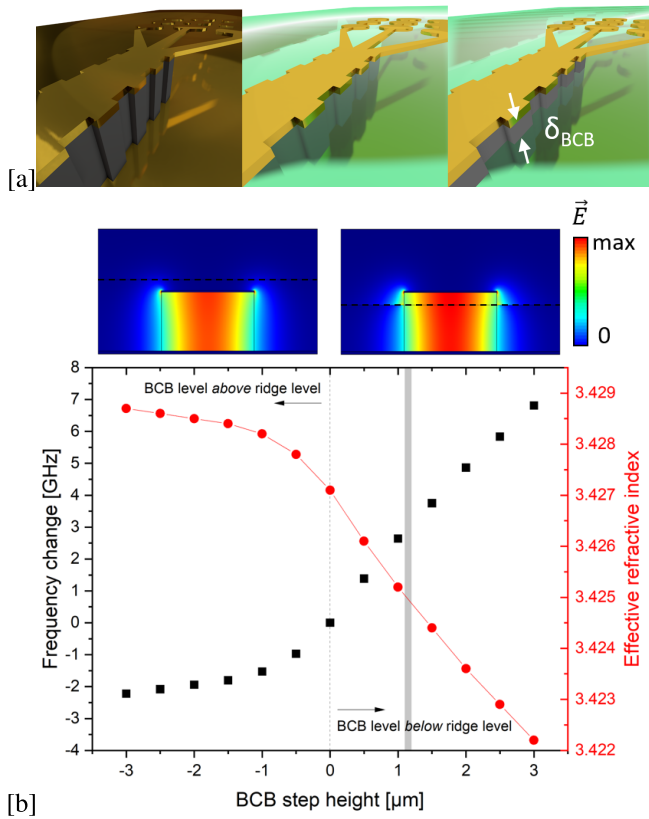
Fig. 5.   a) Model of the front mirror. Left: structure with BCB not shown, for clarity. Center: ideal case, with BCB at the same height as the etched structure. Right: realistic case, where BCB is overetched and δ_{BCB} appears. b) Frequency tuning simulation by changing the relative level of BCB surrounding the laser. The change in effective refractive index of the optical mode is indicated on the right y-axis. The diagrams above show the optical mode for the BCB level above and below the ridge level, respectively (calculated quantity is the electric field, present only in the vertical polarization within the metal-metal waveguide).
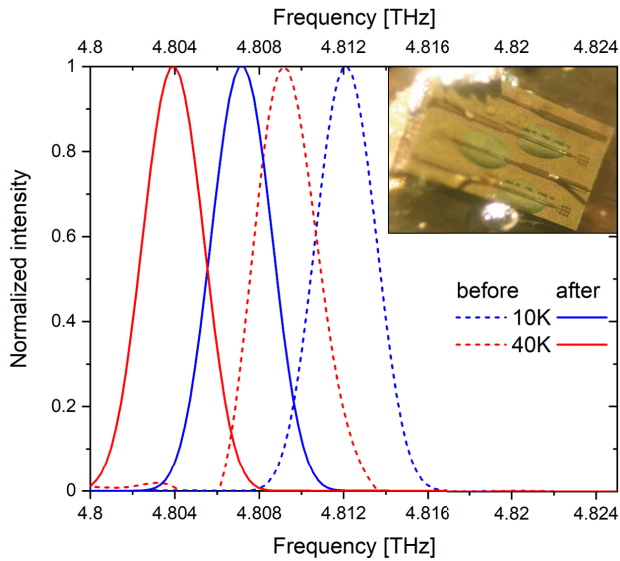

Fig. 6.   Spectrum measurements before and after applying the BCB over the laser. A frequency shift of about 5GHz is visible at both 10K and 40K. Inset: optical microscope image of overcoating the front reflector with the BCB dielectric.

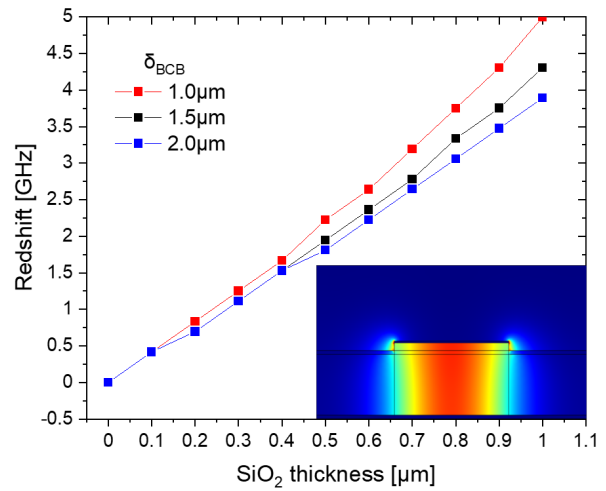evaporating roughly 500nm of SiO_2 over the whole mounted sample.

Fig. 7.   Simulated redshift due to added layer of silicon dioxide to partially refill the space left after overetching the BCB. Inset shows the optical mode with a positive δ_{BCB} and a layer of dioxide deposited on top.
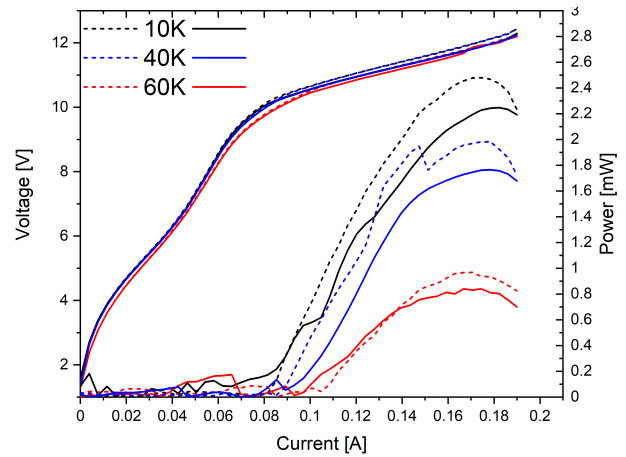

Fig. 8.   L-I-V curves of a laser before (dashed lines) and after (solid lines) SiO2 deposition by electron beam evaporation. The voltage is virtually unchanged, while the dielectric over the antenna causes the power to decrease by roughly the same amount at different temperatures.

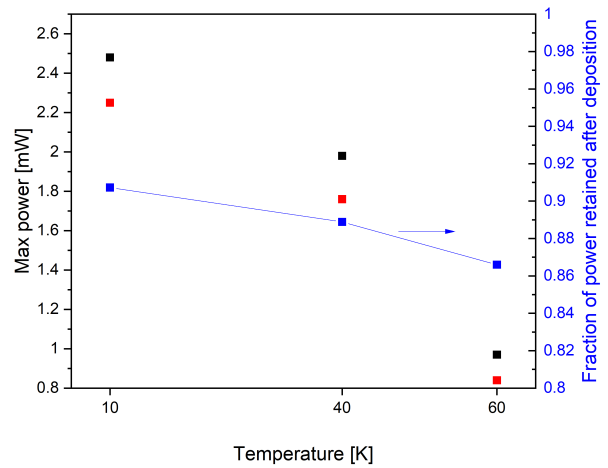Fig. 9.   Lasers retain about 90% of the emitted power after depositing a 500nm-thick layer of silicon dioxide. The effect is more apparent at higher temperatures. An obvious improvement can be obtained by shielding the antennas before deposition, e.g. with photoresist, and then removing it to uncover the metal.

It can be seen in Fig. 8 that while the I-V curve does not change, the power decreases. This is due to the dielectric
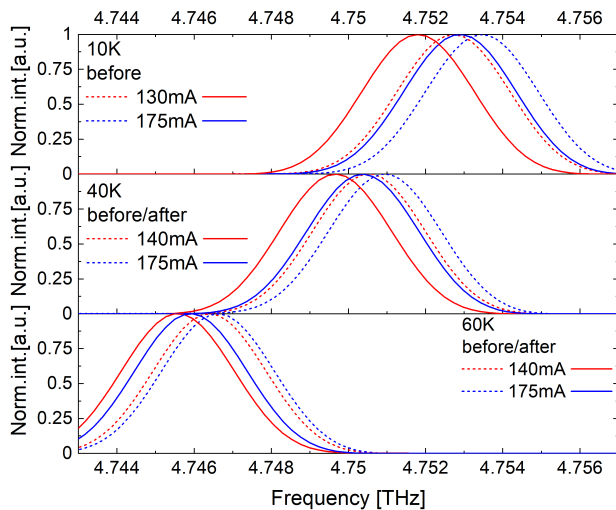
Fig. 10. Spectrum measurements before and after deposition of silicon dioxide. A tuning of 1 GHz is visible. This method offers a platform for arbitrary tunability, by changing the thickness and material used.

layer that is now covering the antenna, thus reducing the light output. Still, about 90% of the power is retained in this manner (see Fig. 9), and even 100% would be possible with a more involved procedure, where the antenna is first shielded with a protective layer, e.g. photoresist, which is later removed.

More interesting, however, are the spectrum measurements (Fig. 10), which reveal a red shift of 1 GHz in the lasing frequency, between before and after the deposition. This effect is about half the magnitude expected from the simulation. We suspect this is due to the main amplifying section not being sensitive to frequency tuning, like the front reflector.

V. CONCLUSION

We have presented a systematic way of searching for a laser with a very specific frequency, using a robust method which accounts for the potential processing uncertainties by covering a larger range of device geometries. In addition, we have shown the performance of such a laser, in particular its tunability in current and temperature, around its intended operation parameters. Finally, we have transformed a processing uncertainty into a method to post-process tune the frequency of lasers that have been fully mounted and measured, by correcting the local geometry or altering it in a customized way, using the refractive index (material) and thickness as tuning parameters.

ACKNOWLEDGMENT

The authors would like to thank Matthias Justen for a fruitful collaboration and Lorenzo Bosco and Urban Senica for insightful discussions.

REFERENCES

[1] S. S. Dhillon, M. S. Vitiello, and E. H. Linfield, "The 2017 terahertz science and technology roadmap," *J. Phys. D., Appl. Phys.*, vol. 50, no. 4, 2017, Art. no. 043001.
[2] N. Palka, "Identification of concealed materials, including explosives, by terahertz reflection spectroscopy," *Opt. Eng.*, vol. 53, no. 3, Dec. 2013, Art. no. 031202.
[3] V. P. Wallace et al., "Terahertz pulsed imaging of basal cell carcinoma ex vivo and in vivo," *Brit. J. Dermatology*, vol. 151, no. 2, pp. 424–432, Aug. 2004.
[4] M. Theuer, S. S. Harsha, D. Molter, G. Torosyan, and R. Beigang, "Terahertz time-domain spectroscopy of gases, liquids, and solids," *ChemPhysChem*, vol. 12, no. 15, pp. 2695–2705, Oct. 2011.
[5] S. Heyminck, U. U. Graf, R. Güsten, J. Stutzki, H. W. Hübers, and P. Hartogh, "GREAT: The SOFIA high-frequency heterodyne instrument," *Astron. Astrophys.*, vol. 542, p. L1, Jun. 2012.
[6] C. Risacher et al., "The upGREAT dual frequency heterodyne arrays for SOFIA," *J. Astronomical Instrum.*, vol. 7, no. 4, Dec. 2018, Art. no. 1840014.
[7] R. T. Boreiko, A. L. Betz, and J. Zmuidzinas, "Heterodyne spectroscopy of the 158 micron CII line in M42," *Astrophysical J.*, vol. 325, pp. 47—51, Feb. 1988.
[8] J. Faist, F. Capasso, D. L. Sivco, C. Sirtori, A. L. Hutchinson, and A. Y. Cho, "Quantum cascade laser," *Science*, vol. 264, no. 5158, pp. 553–556, 1994.
[9] R. Köhler et al., "Terahertz semiconductor-heterostructure laser," *Nature*, vol. 417, no. 6885, pp. 156–159, 2002.
[10] K. Ohtani et al., "High performance 4.7 THz GaAs quantum cascade lasers based on four quantum wells," *New J. Phys.*, vol. 18, no. 12, 2016, Art. no. 123004.
[11] D. Turčinková et al., "Electrically tunable terahertz quantum cascade lasers based on a two-sections interdigitated distributed feedback cavity," *Appl. Phys. Lett.*, vol. 106, no. 13, 2015, Art. no. 131107.
[12] H.-W. Hübers et al., "Terahertz quantum cascade laser as local oscillator in a heterodyne receiver," *Opt. Exp.*, vol. 13, no. 15, pp. 5890–5896, 2005.
[13] L. Schrottke et al., "Quantum-cascade lasers as local oscillators for heterodyne spectrometers in the spectral range around 4.745 THz," *Semicond. Sci. Technol.*, vol. 28, Feb. 2013, Art. no. 035011.
[14] H. Richter, M. Wienold, L. Schrottke, K. Biermann, H. T. Grahn, and H. Hübers, "4.7-THz local oscillator for the GREAT heterodyne spectrometer on SOFIA," *IEEE Trans. Terahertz Sci. Technol.*, vol. 5, no. 4, pp. 539–545, Jul. 2015.
[15] J. L. Kloosterman et al., "Hot electron bolometer heterodyne receiver with a 4.7-THz quantum cascade laser as a local oscillator," *Appl. Phys. Lett.*, vol. 102, no. 1, Jan. 2013, Art. no. 011123.
[16] H. Richter et al., "Observation of atomic oxygen in the mesosphere and thermosphere of Earth with the THz heterodyne spectrometer GREAT," in *Proc. 46th Int. Conf. Infr., Millim. Terahertz Waves (IRMMW-THz)*, Aug. 2021, pp. 1–2.
[17] J. R. Gao et al., "Terahertz heterodyne receiver based on a quantum cascade laser and a superconducting bolometer," *Appl. Phys. Lett.*, vol. 86, no. 24, Jun. 2005, Art. no. 244104.
[18] A. Khalatpour, J. L. Reno, and Q. Hu, "Phase-locked photonic wire lasers by π coupling," *Nature Photon.*, vol. 13, no. 1, pp. 47–53, Jan. 2019.
[19] Y. Jin, J. L. Reno, and S. Kumar, "Phase-locked terahertz plasmonic laser array with 2 W output power in a single spectral mode," *Optics*, vol. 7, no. 6, pp. 708–715, 2020.
[20] M. Wienold, A. Semenov, H. Richter, and H.-W. Hübers, "A balloon-borne 4.75 THz-heterodyne receiver to probe atomic oxygen in the atmosphere," in *Proc. 45th Int. Conf. Infr., Millim., Terahertz Waves (IRMMW-THz)*, Nov. 2020, pp. 1–2.
[21] D. J. Hayton et al., "A 4.7 THz HEB/QCL heterodyne receiver for STO-2," in *Proc. 39th Int. Conf. Infr., Millim., Terahertz Waves (IRMMW-THz)*, Sep. 2014, pp. 1–2.
[22] A. Valavanis et al., "Development of terahertz quantum-cascade lasers for satellite-borne measurement of key gas species," in *Proc. Conf. Lasers Electro-Optics (CLEO)*, May 2019, pp. 1–2.
[23] A. Khalatpour et al., "A tunable unidirectional source for GUSTO's local oscillator at 4.74 THz," *IEEE Trans. Terahertz Sci. Technol.*, vol. 12, no. 2, pp. 144–150, Mar. 2022.
[24] S. Fathololoumi, E. Dupont, and C. Chan, "Terahertz quantum cascade lasers operating up to ∼200 K with optimized oscillator strength and improved injection tunneling," *Opt. Exp.*, vol. 20, no. 4, pp. 3866–3876, 2012.
[25] L. Bosco et al., "Thermoelectrically cooled THz quantum cascade laser operating up to 210 K," *Appl. Phys. Lett.*, vol. 115, no. 1, 2019, Art. no. 010601.
[26] A. Khalatpour, A. K. Paulsen, C. Deimert, Z. R. Wasilewski, and Q. Hu, "High-power portable terahertz laser systems," *Nature Photon.*, vol. 15, no. 1, pp. 16–20, Jan. 2021.

[27] R. T. Boreiko and A. L. Betz, "Heterodyne spectroscopy of the 63 μm O I line in M42," *Astrophysical J.*, vol. 325, no. 1, p. L83, 1996.

[28] D. Büchel et al., "4.7-THz superconducting hot electron bolometer waveguide mixer," *IEEE Trans. Terahertz Sci. Technol.*, vol. 5, no. 2, pp. 207–214, Mar. 2015.

[29] M. I. Amanti et al., "Bound-to-continuum terahertz quantum cascade laser with a single-quantum-well phonon extraction/injection stage," *New J. Phys.*, vol. 11, no. 12, Dec. 2009, Art. no. 125022.

[30] D. Turčinková et al., "Ultra-broadband heterogeneous quantum cascade laser emitting from 2.2 to 3.2 THz," *Appl. Phys. Lett.*, vol. 99, no. 19, 2011, Art. no. 191104.

[31] C. Bonzon, I. C. B. Chelmus, K. Ohtani, M. Geiser, M. Beck, and J. Faist, "Integrated patch and slot array antenna for terahertz quantum cascade lasers at 4.7 THz," *Appl. Phys. Lett.*, vol. 104, no. 16, Apr. 2014, Art. no. 161102.

[32] M. Rösch, G. Scalari, M. Beck, and J. Faist, "Octave-spanning semi-conductor laser," *Nature Photon.*, vol. 9, no. 1, pp. 42–47, Jan. 2015.

[33] L. Bosco, C. Bonzon, K. Ohtani, M. Justen, M. Beck, and J. Faist, "A patch-array antenna single-mode low electrical dissipation continuous wave terahertz quantum cascade laser," *Appl. Phys. Lett.*, vol. 109, no. 20, Nov. 2016, Art. no. 201103.

[34] L. A. Dunbar, R. Houdré, G. Scalari, L. Sirigu, M. Giovannini, and J. Faist, "Small optical volume terahertz emitting microdisk quantum cascade lasers," *Appl. Phys. Lett.*, vol. 90, no. 14, Apr. 2007, Art. no. 141114.

[35] K. Unterrainer et al., "Quantum cascade lasers with double metal-semiconductor waveguide resonators," *Appl. Phys. Lett.*, vol. 80, no. 17, pp. 3060–3062, Apr. 2002.

[36] B. S. Williams, S. Kumar, H. Callebaut, Q. Hu, and J. L. Reno, "Ter-ahertz quantum-cascade laser at $\lambda \approx 100$ μm using metal waveguide for mode confinement," *Appl. Phys. Lett.*, vol. 83, no. 11, pp. 2124–2126, Sep. 2003.

[37] U. Senica et al., "Planarized THz quantum cascade lasers for broadband coherent photonics," 2022, *arXiv:2207.06737*.

[38] H. Zhang, G. Scalari, J. Faist, L. A. Dunbar, and R. Houdré, "Design and fabrication technology for high performance electrical pumped terahertz photonic crystal band edge lasers with complete photonic band gap," *J. Appl. Phys.*, vol. 108, no. 9, Nov. 2010, Art. no. 093104.

[39] M. Justen, C. Bonzon, K. Ohtani, M. Beck, and J. Faist, "2D patch antenna array on a double metal quantum cascad laser with >90% coupling to a Gaussian beam and selectable facet transparency at 1.9 THz," *Opt. Exp.*, vol. 41, no. 19, pp. 4590–4592, 2016.

[40] D. Turčinkova, M. I. Amanti, F. Castellano, M. Beck, and J. Faist, "Continuous tuning of terahertz distributed feedback quantum cascade laser by gas condensation and dielectric deposition," *Appl. Phys. Lett.*, vol. 102, no. 18, May 2013, Art. no. 181113.

[41] B. Mirzaei et al., "Frequency tuning of third-order distributed feedback terahertz quantum cascade lasers by SiO$_2$ and PMMA," *IEEE Trans. Terahertz Sci. Technol.*, vol. 6, no. 6, pp. 851–857, Nov. 2016.

Tudor Olariu was born in Romania. He received the B.Sc. degree from Jacobs University, Bremen, Germany, in 2014, the joint M.Sc. degree from Aix-Marseille Université, France, and the Karlsruhe Institute of Technology, Germany, in 2016. He was awarded the Ph.D. degree from the Swiss Institute of Technology (ETH), Zurich, Switzerland in 2023, for his work on THz quantum cascade lasers as local oscillators for astronomy, in the group of Prof. Jerome Faist.

Mattias Beck was born in Switzerland. He received the M.S. degree in physics from the Swiss Institute of Technology (ETH), Zürich, Switzerland, in 1991, and the Ph.D. degree in technical sciences from the Swiss Institute of Technology, Lausanne, Switzerland, in 1997. His studies were focused on the growth and characterization of strained InAlAs-InGaAs heterostructures for high-frequency applications. He was with the Bell Laboratories, Lucent Technologies, Murray Hill, NJ, USA, in 1997, where his work focused on the growth of buried heterostructure quantum-cascade lasers. He joined the Group of Prof. J. Faist, University of Neuchâtel, Neuchâtel, Switzerland, in October 1997, where he was involved in the molecular beam epitaxy growth of quantum-cascade lasers. In 2007, he became a Senior Researcher with the Quantum Optoelectronics Group, ETH Zürich.

Jérôme Faist (Fellow, IEEE) was born in Switzerland. He received the Ph.D. degree in physics from the Swiss Institute of Technology, Lausanne, Switzerland, in 1989. From 1989 to 1991, he was with IBM Rueschlikon. From 1991 to 1997, he was with the Bell Laboratories. He was a Full Professor with the Physics Institute, University of Neuchâtel, in 1997. He was a Full Professor with ETH Zürich, in 2007. His current research interests include the development of mid-infrared and terahertz quantum cascade lasers and frequency combs and the physics of ultrastrong light-matter coupling in metamaterial resonators. He was a recipient of numerous awards for his key contribution to the development of the quantum cascade laser, including the IEEE/LEOS William Streifer Award for Scientific Achievement and the National Swiss Latsis Prize in 2002.